Diamagnetic stabilization of ideal ballooning modes in the edge pedestal

B. N. Rogers and J. F. Drake
Institute for Plasma Research, University of Maryland, College Park, Maryland 20742

(Received 3 March 1999; accepted 2 April 1999)

The stability of the tokamak edge pedestal to ballooning modes is addressed using three-dimensional simulations of the Braginskii equations and simple analytic models. The effects of ion diamagnetic drift and the finite radial localization of the pedestal pressure gradient are found to be strongly stabilizing when $\delta < \delta_R$, where δ is the pedestal half-width and $\delta_R \sim \rho_i^{2/3} R^{1/3}$ in the center of the pedestal. In this limit, conventional ballooning modes within the pedestal region become stable, and a stability condition is obtained in the two fluid system $\alpha/\alpha_c < (4/3)\delta_R/\delta$ (stable) which is much less stringent than that predicted by local magnetohydrodynamic (MHD) theory $(\alpha/\alpha_c < 1)$. Given $\alpha \sim q^2 R\beta/\delta$, this condition implies a stability limit on the pedestal β: $\beta < \beta_c$, where $\beta_c = (4\alpha_c/3q^2)\delta_R/R$. This limit is due the onset of an ideal pressure driven ''surface'' instability that depends only on the pressure drop across the pedestal. Near marginal conditions, this mode has a poloidal wavenumber $k_\theta \sim 1/\delta_R$, a radial envelope $\sim \delta_R(>\delta)$, and real frequency $\omega \sim c_s/\sqrt{\delta_R R}$. © *1999 American Institute of Physics.* [S1070-664X(99)03007-4]

I. INTRODUCTION

Magnetohydrodynamic (MHD) analyses of data from DIII-D (Ref. 1) and other tokamaks indicate the steep gradient region of an *H*-mode (high confinement mode) edge pedestal may well exceed the first ideal stability boundary for ballooning modes. Recent efforts to resolve this apparent discrepancy have focused on the stabilizing effects of the edge bootstrap current.[1] We propose here an alternate explanation, based on three-dimensional simulations of the Braginskii equations and the study of some simple analytic models. We find a substantial enhancement of ballooning mode stability relative to ideal MHD theory can be explained by a two-fluid stability analysis that accounts for both ion diamagnetic effects and the strong radial localization of the edge pedestal pressure gradient. Our results suggest these effects, at typical *H*-mode parameters, can allow ideal ballooning modes of all wavelengths to remain stable even well above the first ideal MHD stability limit. Long wavelength modes with $k_\theta\delta \ll 1$ (δ being the pedestal half-width) remain stable because the radial localization of the pedestal gradient greatly weakens the drive of such modes relative to the stabilizing contribution of magnetic line-bending. Shorter wavelength modes with $k_\theta\delta \gtrsim 1$, on the other hand, are strongly stabilized by the competitive contributions of ω_{*i} and $E\times B$ shear effects. The key parameter that determines the importance of nonideal effects is the normalized ion diamagnetic velocity $\hat{v}_{*i} = V_{*i}/(\gamma_b\delta)$, where $V_{*i} = \rho_i^2\Omega_{ci}/L_{p_i}$ and $\gamma_b = [2c_s^2/(L_p R)]^{1/2}$ (with $c_s^2 = P/\rho$) are the local values of the ion diamagnetic velocity and inverse ideal ballooning time at the center of the pedestal. Assuming $L_p \sim L_{p_i} \sim \delta$, $\hat{v}_{*i}$ can be written as

$$\hat{v}_{*i} = \left(\frac{\delta_R}{\delta}\right)^{3/2}, \quad \delta_R = \left(\frac{T_i}{2(T_i+T_e)}\right)^{1/3} \rho_i^{2/3} R^{1/3}. \tag{1}$$

For $\hat{v}_{*i} \ll 1$ $(\delta \gg \delta_R)$, the stability boundary of the two fluid system, represented in Fig. 1(a) by the solid line, is the same as that predicted by ideal MHD theory $(\alpha/\alpha_c = 1)$. For $\hat{v}_{*i} \sim 1$, however, the two fluid stability limit increases almost linearly with $\hat{v}_{*i}$, exceeding the ideal MHD limit by about a factor of 2 when $\hat{v}_{*i} \sim 1$. Since the condition $\hat{v}_{*i} \gtrsim 1$ is satisfied in the *H*-mode pedestal of many present day tokamak discharges (in DIII-D,[1] for example, we obtain $\hat{v}_{*i} \sim 2$ given $\delta \sim 4\rho_i \sim 0.004R$) this may explain the apparent ability of pedestal gradient in some experiments to exceed the ideal limit.

In the regime $\hat{v}_{*i} > 1$, one would not expect a stability limit like that in Fig. 1(a), or any stability limit at all for that matter, to arise from conventional ballooning modes, i.e., ballooning modes that are radially localized within the pedestal region. As shown below, this is because such localized modes necessarily have short poloidal wavelengths $k_\theta\delta \gtrsim 1$, and thus have typical diamagnetic frequencies $\omega_{*i} \gtrsim V_{*i}/\delta$ that, in the regime $\hat{v}_{*i} > 1$, always exceed the largest possible ballooning mode growth rate obtainable from local MHD theory, $\gamma_{\max} \sim \gamma_b$. Similarly, assuming the poloidal $E\times B$ and diamagnetic flows balance[2] $V_E \sim V_{*i}$ (a result consistent with the simulations discussed later), the typical $E\times B$ shearing rate in the pedestal $\gamma_E \sim V_E' \sim V_{*i}/\delta$ also exceeds $\gamma_{\max}$ given $\hat{v}_{*i} > 1$. Consistent with this, the modes leading to the stability boundary in Fig. 1(a) for $\hat{v}_{*i} > 1$ are not localized modes, i.e., they have poloidal wavelengths and radial envelopes that are larger than the pedestal width. Unlike conventional ballooning modes, furthermore, the stability and eigenfrequencies of these long wavelength instabilities are insensitive to the details of the pedestal structure, and depend only on the plasma pressure drop across the pedestal. The consistency of this with Fig. 1(a) can be understood from the analytic form of the stability boundary that we obtain later in the asymptotic limit $\hat{v}_{*i} \gg 1$ [see Fig. 1(a), dotted–dashed line],

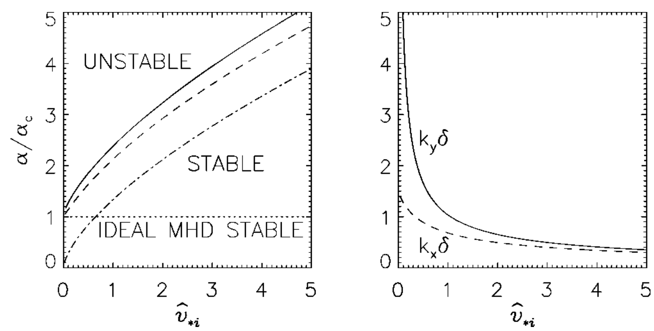

FIG. 1. (a) Stability boundaries for ideal ballooning modes. (b) Wave numbers of marginally stable mode for ramp profile.

$$\frac{\alpha}{\alpha_c}<\frac{4}{3}\hat{v}_{*i}^{2/3}\equiv\frac{4}{3}\frac{\delta_R}{\delta}\quad(\text{stable}). \tag{2}$$

With the substitution $\alpha\simeq q^2R\beta/\delta$, the pedestal scale length δ drops out of this condition, leading to the (δ independent) stability condition on the pedestal β for $\hat{v}_{*i}\gg 1$,

$$\beta<\beta_c\equiv\frac{4\alpha_c}{3q^2}\frac{\delta_R}{R}=\frac{4\alpha_c}{3q^2}\left(\frac{T_i}{2(T_i+T_e)}\right)^{1/3}\left(\frac{\rho_i}{R}\right)^{2/3}\quad(\text{stable}). \tag{3}$$

Physically, the limiting mode in this case is analogous to the instability of a light fluid supporting a heavy fluid against gravity, that is, the sharp boundary limit of the Raleigh–Taylor instability. Such sharp boundary modes, in either the case of Raleigh–Taylor or ballooning modes, can be obtained from the analogous dispersion relation for local modes in diffuse profiles by a simple prescription, namely, by replacing the inverse profile scale lengths $1/L_\rho=|\rho'/\rho|$, $1/L_P=|P'/P|$, etc. by the wave number along the boundary. In the ballooning mode case this substitution gives $\gamma^2=\gamma_b^2\equiv 2c_s^2/(RL_p)\rightarrow\gamma_k^2$ with $\gamma_k^2\equiv 2c_s^2k/R$, which is identical to the dispersion relation we obtain later for the unstable modes associated with Eq. (3) if the stabilizing contributions of ω_{*i} and magnetic line bending are neglected. Similarly, with $|P_i'/P_i|\rightarrow k$, one finds $\omega_{*i}^2\rightarrow(k\delta_R)^3\gamma_k^2$. The scale length δ_R is therefore introduced into the problem through the addition of diamagnetic effects, which cutoff the monotonic increase of $\gamma\propto\sqrt{k}$ at $k\sim 1/\delta_R$, and result in the maximum growth rate $\gamma\sim\gamma_R=2c_s^2/(\delta_RR)$. Finally, these fastest modes are stabilized by the addition of line bending effects if $\gamma_R^2\lesssim V_A^2/(qR)^2$, or equivalently $\beta\lesssim\delta_R/(q^2R)$, consistent with Eq. (3).

We first describe the Braginskii model on which our simulations are based in Sec. II. In Sec. III, we describe a simulation of the evolution of the edge pedestal in the context of the L–H (low–high) transition model of Ref. 3. In Sec. IV, we describe the two-fluid stability analyses of some simple analytic models which are qualitatively consistent with the behavior of the simulations. In Sec. V, we summarize our main conclusions.

II. MODEL

The simulations are carried out in a poloidally and radially localized, flux-tube domain that winds around the torus.[4] Assuming a shifted-circle magnetic geometry, the nonlinear equations for perturbations of the magnetic flux $\tilde{\psi}$, electric potential $\tilde{\phi}$, density $\tilde{n}$, electron and ion temperatures $\tilde{T}_e$, $\tilde{T}_i$, and parallel flow $\tilde{v}_\parallel$ are

$$\hat{\alpha}[\partial_t\tilde{\psi}+\alpha_d(1+1.71\eta_e)\partial_y\tilde{\psi}]-\nabla_\parallel[\tilde{\phi}-\alpha_d(\tilde{p}_e+0.71\tilde{T}_e)]=\tilde{J}, \tag{4}$$

$$\nabla_\perp\cdot d_t\nabla_\perp(\tilde{\phi}+\tau\alpha_d\tilde{p}_i)+\hat{C}(\tilde{p}+\tilde{G})-\nabla_\parallel\tilde{J}=0, \tag{5}$$

$$d_t\tilde{n}+\partial_y\tilde{\phi}-[\epsilon_n\hat{C}(\tilde{\phi}-\alpha_d\tilde{p}_e)-\epsilon_v\nabla_\parallel\tilde{v}_\parallel+\alpha_d\epsilon_n(1+\tau)\nabla_\parallel\tilde{J}]=0, \tag{6}$$

$$d_t\tilde{T}_i+\eta_i\partial_y\tilde{\phi}-\tfrac{2}{3}[\epsilon_n\hat{C}(\tilde{\phi}-\alpha_d\tilde{p}_e+\tfrac{5}{2}\tau\alpha_d\tilde{T}_i)-\epsilon_v\nabla_\parallel\tilde{v}_\parallel+\alpha_d\epsilon_n(1+\tau)\nabla_\parallel\tilde{J}]-\tfrac{2}{3}\kappa_i\nabla_\parallel(\nabla_\parallel\tilde{T}_i+\hat{\alpha}\eta_i\partial_y\tilde{\psi})=0, \tag{7}$$

$$d_t\tilde{T}_e+\eta_e\partial_y\tilde{\phi}-\tfrac{2}{3}[\epsilon_n\hat{C}(\tilde{\phi}-\alpha_d\tilde{p}_e-\tfrac{5}{2}\alpha_d\tilde{T}_e)-\epsilon_v\nabla_\parallel\tilde{v}_\parallel+1.71\alpha_d\epsilon_n(1+\tau)\nabla_\parallel\tilde{J}]-\tfrac{2}{3}\kappa_e\nabla_\parallel(\nabla_\parallel\tilde{T}_e+\hat{\alpha}\eta_e\partial_y\tilde{\psi})=0, \tag{8}$$

$$d_t\tilde{v}_\parallel=-\epsilon_v[\nabla_\parallel(\tilde{p}+4\tilde{G})+(2\pi)^2\alpha\partial_y\tilde{\psi}], \tag{9}$$

where $\nabla_\parallel=\partial_z+\hat{\alpha}\mathbf{z}\times\nabla_\perp\tilde{\psi}\cdot\nabla_\perp$, $d_t=\partial_t+\mathbf{z}\times\nabla_\perp\tilde{\phi}\cdot\nabla_\perp$, $\nabla_\perp^2=(\partial_x+\Lambda(z)\partial_y)^2+\partial_y^2$, $\hat{C}=(\cos(2\pi z)+\Lambda(z)\sin(2\pi z)-\epsilon)\partial_y+\sin(2\pi z)\partial_x$, $\Lambda(z)=2\pi\hat{s}z-\alpha\sin(2\pi z)$, $\tilde{G}=2\gamma_p[\hat{C}(\tilde{\phi}+\tau\alpha_d\tilde{p}_i),-4(\epsilon_v/\epsilon_n)\nabla_\parallel\tilde{v}_\parallel]$, $\tilde{J}=\nabla_\perp^2\tilde{\psi}$, $\tilde{p}_\alpha=\tilde{n}+\tilde{T}_\alpha$, $\tilde{p}=(\tilde{p}_e+\tau\tilde{p}_i)/(1+\tau)$. The time ($t$), perpendicular ($x$,$y$) and parallel ($z$) normalization scales are $t_0=(RL_n/2)^{1/2}/c_s$, $L_0=2\pi q_a(n_0e^2\eta_\parallel\rho_sR/m_i\omega_{ci})^{1/2}(2R/L_n)^{1/4}$, and $L_z=2\pi q_aR$, with an associated diffusion rate $D_0=L_0^2/t_0$. The diamagnetic and MHD parameters are

$$\alpha_d=\frac{\rho_sc_st_0}{(1+\tau)L_nL_0},\quad \alpha=q_a^2R\frac{8\pi(p_{e0}+p_{i0})}{B^2L_p}. \tag{10}$$

Other parameters are $\tau=T_{i0}/T_{e0}$, $\eta_\alpha=L_n/L_{T_\alpha}$, $\epsilon=a/R$, $\epsilon_n=2L_n/R$, $\epsilon_v=\epsilon_n^{1/2}/(4\pi q_a)$, $\hat{\alpha}=(2\pi)^2\alpha L_p/L_n$, $L_n/L_p=[1+\eta_e+\tau(1+\eta_i)]/(1+\tau)$, $\kappa_e=1.6\alpha_d^2\epsilon_n(1+\tau)$, $\kappa_i=0.064(m_p/m_i)^{1/2}\tau^{5/2}\alpha_d^2\epsilon_n(1+\tau)$, $\gamma_p=0.16\pi^2q_a^2\kappa_i$. The parallel coordinate values $z=0$ and $z=\pm 1/2$ represent the outboard and inboard midplanes, respectively. The transverse flux coordinates x,y correspond to local radial and poloidal variables. Unless noted otherwise, we consider the values $\hat{s}=1$, $\tau=1$, $\epsilon_n=0.02$, $\epsilon=0.2$, $q_a=3$, $\eta_i=\eta_e=1$, $m_i/m_p=2$.

III. SIMULATION RESULTS

The present study extends the investigation of pedestal stability begun in our earlier work,[3] so we begin this section with a brief review of some past results. We argue in Ref. 3 that the L–H transition, and thus the formation of the edge pedestal, is linked to the dependence of the turbulent edge transport on the MHD and diamagnetic parameters α, α_d. In

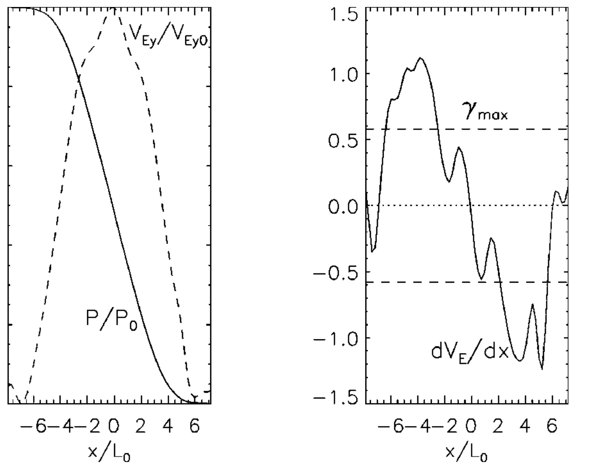

FIG. 2. Pressure (a, solid), V_{Ey} (a, dashed), and dV_{Ey}/dx (b, solid) profiles.

the regime of higher $\alpha_d \sim 1$, small but finite values of α lead to a strong suppression of transport, and as a result, in this regime a local increase in the plasma pressure gradient, above a threshold in α, causes a *reduction* of the transport. In the presence of a fueling source, this reversed dependence of the transport on the gradient makes it impossible for the system to maintain transport equilibrium, and leads to a spontaneous steepening of the profiles above thresholds in α and α_d that we associate with the $L-H$ transition.

We simulated this transition in Ref. 3 in the context of a simple model. The model includes a source and sink (radially periodic) in the density Eq. (6), intended to represent neutral particle fueling in the edge. In response to the source, a modulation of the density profile forms that steepens the gradient in the center of the simulation domain. The strength of the source is chosen so that for $\alpha_d \sim 1$ and $\alpha \ll 1$ the source produces only a slight steepening of the profile before the system comes into equilibrium. The MHD parameter α is then slowly increased with time. With increasing α the transport drops and the source causes the gradient to steepen, enhancing the turbulence until a new equilibrium is reached. At a critical value of α, the $L-H$ threshold condition is crossed and the pressure profile spontaneously begins to steepen [see Fig. 2(a), solid line]. This steepening leads to the formation of a sheared poloidal $\mathbf{E}\times\mathbf{B}$ flow [Fig. 2(a), dashed line] which balances the poloidal ion diamagnetic drift.

As was mentioned in Ref. 3, the steepening of the profiles following the transition in the simulations is not limited by the ideal $n\rightarrow\infty$ stability boundary. This is the case for the profile in Fig. 2(a), which is a plot of the ion pressure profile roughly $1000t_0$ after the transition in a simulation with $\epsilon_n = 0.02$, $\alpha_d = 1$. The α-value at the center of the pedestal, $\alpha(x=0)=1.6$, is well beyond the first stability limit ($\alpha = 0.8$ at $\hat{s}=1$). Shortly after the time of Fig. 2, however, the onset of a rapidly growing global mode with $k_y = 0.4$ (poloidal wavelength equal to the box-size) in the steep gradient region leads finally to a complete disruption of the pedestal, see Fig. 3. Global mode activity begins early in the simulation and appears at first in the form of two weakly growing modes. These modes, one of which propagates in the ω_{*e} direction and the other in the ω_{*i} direction, resemble the two dominant linear resistive ballooning modes in our system at $k_y = 0.4$. The ω_{*i} root eventually transitions to the rapidly growing instability that destroys the pedestal. The time evolution of the poloidally averaged ion heat flux during the sequence of events prior to the pedestal crash is shown in Fig. 4. The large initial drop in the flux ($t/t_0 \sim 1100-1300$) represents the transition. After this, coherent mode activity in the pedestal leads to weakly growing, rapid oscillations (mostly at $\omega \sim \omega_{*e}$) for $t/t_0 > 1600$, followed by a rapid crash phase at $t/t_0 \sim 2300-2350$.

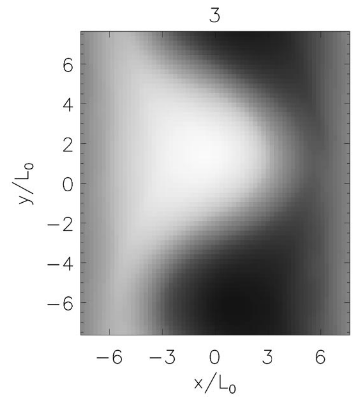

FIG. 3. Global mode leading to the pedestal crash.

As noted earlier, given the balance that exists in pedestal between $V_{E\times B}$ and V_{*i}, the stabilizing contribution due to $E\times B$ shear is generally competitive with that of the ion diamagnetic drift for global $k_y \sim 1/\delta$ modes. The $E\times B$ shear effect alone, however, is not sufficient to explain the stability of the simulations, since the actual $\mathbf{E}\times\mathbf{B}$ shear vanishes in the center of the pedestal where the ion-diamagnetic component of the flow (and thus $V_{E\times B}$) has a maximum. In the case $\hat{v}_{*i} \sim 1$, which applies to the simulation just described at later times, this results in a region, comparable to the half-width of the pedestal, in which the $\mathbf{E}\times\mathbf{B}$ shearing rate is too small to account for the absence of ideal modes. This is demonstrated in Fig. 2(b), which compares the local $\mathbf{E}\times\mathbf{B}$ shearing rate (solid) in the pedestal of Fig. 2(a) with the maximum ideal MHD ballooning mode growth rate (dashed).

If we attribute the weakly growing modes following the transition to nonideal (e.g., resistive) effects, the behavior of

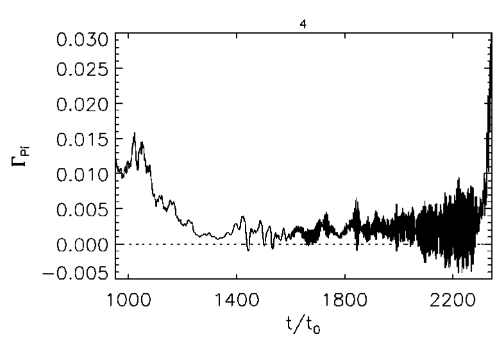

FIG. 4. Normalized ion heat flux vs t/t_0.

the simulations is qualitatively consistent with Fig. 1(a). The steepening of the pedestal gradient following the transition leads to a trajectory in the $\alpha-\hat{v}_{*i}$ space of Fig. 1(a) that eventually intersects the unstable region near $\alpha\sim 2\alpha_{\rm crit}$ (where $\hat{v}_{*i}\sim 1$). Thus, Fig. 1(a) is consistent with the apparent onset of an ideal mode in the simulations at such a value of α. We therefore now turn to the analysis leading to Fig. 1(a).

IV. ANALYTIC MODELS

We now explore the stability of ideal ballooning modes in the presence of a radially localized gradient in the context of some simple analytic models. To be consistent with the pedestal simulations discussed above, we assume the equilibrium $E\times B$ and ion-diamagnetic flows balance, $V_{Ey}=-V_{*iy}=-(c/neB)dP_i/dx$. As a further simplification we eliminate the z-dependence of the configuration by taking the magnetic curvature vector as $\boldsymbol{\kappa}=-\hat{e}_x/R$ (bad curvature everywhere) and $\hat{s}=0$, and in analogy to ballooning modes consider modes varying as $\exp(\gamma t+ik_yy+ik_zz)$ with $k_z\equiv\sqrt{\alpha_c}/qR$ fixed (here α_c is a constant of order unity, the meaning of which will be made clear below). Finally, we exclude resistive modes by dropping the resistive term (J term) in Ohm's Law (4), and neglect the (small) terms proportional to ϵ_n, ϵ_v, and γ_p. With these simplifications, Eqs. (4), (5), (6) may be combined to yield (returning to unnormalized units for clarity),

$$\partial_x\left[\left(\rho\gamma\gamma_*+\frac{B^2k_z^2}{4\pi}\right)\partial_x\tilde{f}(x)\right]=k_y^2\left(\rho\gamma\gamma_*+\frac{B^2k_z^2}{4\pi}+\frac{2}{R}\frac{dP}{dx}\right)\tilde{f}(x), \tag{11}$$

where $\gamma_*=\gamma-ik_y(c/neB)dP_i/dx$, $\tilde{f}=\tilde{\phi}/\gamma_*$. Now introducing the normalizations

$$\hat{x}=\frac{x}{\delta_0},\quad \hat{k}_y=k_y\delta_0,\quad \hat{\rho}=\frac{\rho}{\rho_0},\quad \hat{P}=\frac{P}{P_0},$$
$$\hat{P}_i=\frac{P_i}{P_{i0}},\quad \hat{\gamma}=\frac{\gamma}{\gamma_0},\quad \gamma_0^2=\frac{2P_0}{\rho_0\delta_0R}, \tag{12}$$

where δ_0, P_0, ρ_0, etc. are (at this stage) arbitrary constants, we obtain

$$\partial_{\hat{x}}[(\hat{\rho}\hat{\gamma}\hat{\gamma}_*+\alpha_c/\alpha_0)\partial_{\hat{x}}\tilde{f}(\hat{x})]=\hat{k}_y^2(\hat{\rho}\hat{\gamma}\hat{\gamma}_*+\alpha_c/\alpha_0+d\hat{P}/d\hat{x})\tilde{f}(\hat{x}), \tag{13}$$

where $\hat{\gamma}_*=\hat{\gamma}-i(\hat{k}_y\hat{v}_{*i0}/\hat{\rho})d\hat{P}_i/d\hat{x}$, $\hat{v}_{*i0}=(\delta_R/\delta_0)^{3/2}$, $\alpha_0=q^2R\beta/\delta_0$ and $\beta\equiv 8\pi P_0/B^2$. In the applications described below we take P_0, ρ_0, etc. to be the values of the corresponding quantities at the center of the pedestal, and with the exception of the step-function pressure profile discussed later, we take $\delta_0=\delta$, the pedestal half-width. With these choices, the constants $\gamma_0\rightarrow\gamma_b$ (the inverse ideal ballooning time), $\alpha_0\rightarrow\alpha$ (the MHD ballooning parameter), and $\hat{v}_{*i0}\rightarrow\hat{v}_{*i}$ [the normalized diamagnetic velocity given by Eq. (1)]. We keep these parameters distinct at this point, however, because the length scale normalization $\delta_0=\delta$ is *not* a natural choice for the instabilities we will obtain in the limit $\hat{v}_{*i}\gg 1$ ($\delta\ll\delta_R$). In this limit, the modes become sensitive only to the pressure drop across the pedestal, and a more natural normalization scale turns out to be $\delta_0=\delta_R$.

As a first example, we consider the profiles $P=P_0(1-\tanh(x/\delta))$, $\rho=\rho_0(1-\tanh(x/\delta))$, $P_i=P_{i0}(1-\tanh(x/\delta))$, or fixing $\delta_0=\delta$: $\hat{P}=\hat{\rho}=\hat{P}_i=1-\tanh(\hat{x})$. Solving Eq. (13) numerically for fixed values of the independent parameters α/α_c and $\hat{v}_{*i}$, and maximizing the growth rate over all $\hat{k}_y$ yields the universal stability diagram (solid curve) shown in Fig. 1(a). As said earlier, for finite $\hat{v}_{*i}$, the ballooning stability limit shown in Fig. 1(a) increases monotonically with $\hat{v}_{*i}$, exceeding the first ideal MHD limit by about a factor of 2 for $\hat{v}_{*i}\sim 1$. To address the physical origin of this curve, we now turn to the analysis of two even simpler models; a finite-ramp profile, which yields the stability boundary shown as the dashed line in Fig. 1(a), and a step-function profile, which leads to the dotted–dashed line.

Turning to the ramp profile, we take $\hat{P}'(\equiv d\hat{P}/d\hat{x})=\hat{P}_i'=-1$ for $-1<\hat{x}<1$, $\hat{P}'=\hat{P}_i'=0$ for $|\hat{x}|>1$, and for simplicity neglect the variation of the density in the inertia term ($\hat{\rho}=1$). The solution for $\tilde{f}(\hat{x})$ that is asymptotically well behaved at large $\hat{x}$ and continuous at $\hat{x}=\pm 1$ is then given by $\tilde{f}=\exp(-|\hat{k}_y|[|\hat{x}|-1])$ for $|\hat{x}|>1$, and $\tilde{f}=\cos(\hat{k}_x x)/\cos(\hat{k}_x)$ for $|\hat{x}|<1$ (even solutions turn out to be the most unstable). Substituting this form into Eq. (13) for $|\hat{x}|<1$ yields

$$\hat{\gamma}\hat{\gamma}_*=\frac{\hat{k}_y^2}{\hat{k}_y^2+\hat{k}_x^2}-\frac{\alpha_c}{\alpha}, \tag{14}$$

where $\hat{k}_x(\equiv k_x\delta)$ is determined by integrating Eq. (13) across $\hat{x}=\pm 1$ as

$$\hat{k}_x\tan(\hat{k}_x)=|\hat{k}_y|\left(\frac{\hat{\gamma}^2+\alpha_c/\alpha}{\hat{\gamma}\hat{\gamma}_*+\alpha_c/\alpha}\right). \tag{15}$$

Solving Eqs. (14), (15) numerically for fixed values of α/α_c and $\hat{v}_{*i}$, and maximizing the growth rate over all $\hat{k}_y$, yields the stability boundary shown as the dashed line in Fig. 1(a). The character of the instability near this threshold can be understood from Fig. 1(b), which shows the corresponding values of $\hat{k}_x$, $\hat{k}_y$ of the marginally stable mode along the stability boundary. In the limit $\hat{v}_{*i}\ll 1$, Fig. 1(b) shows that $\hat{k}_y\gg 1$, $\hat{k}_x\sim 1$. This is consistent with Eq. (15), which for $\hat{k}_y\gg 1$ reduces to $\hat{k}_x\approx\pi/2$. As a result, Eq. (14) becomes $\hat{\gamma}\hat{\gamma}_*\simeq 1-\alpha_c/\alpha-(\pi/2\hat{k}_y)^2$, which for $\hat{v}_{*i}=0$ and $\hat{k}_y\rightarrow\infty$ leads to the maximum growth rate $\hat{\gamma}_0^2=1-\alpha_c/\alpha$, and thus instability for $\alpha>\alpha_c$. For small but finite $\hat{v}_{*i}\ll 1$, the most unstable mode occurs for large but finite $\hat{k}_y\simeq\sqrt{\pi/\hat{v}_{*i}}$, and the usual ω_{*i} stability condition ($\omega_{*i}>2\gamma$) for this fastest mode leads to the overall stability condition $\alpha/\alpha_c<1+\pi\hat{v}_{*i}/2$, which is consistent with the small-$\hat{v}_{*i}$ behavior of the dashed line in Fig. 1(a). Physically, large $\hat{k}_y\gg 1$ is favorable for instability because the mode in this limit becomes strongly localized to the region $|\hat{x}|<1$, thus maximizing its presence in the region where the drive is finite, while minimizing the stabilizing contribution of magnetic line bending in the exterior region $|\hat{x}|>1$. Large $\hat{k}_y \gg 1$ is linked to the regime $\hat{v}_{*i} \ll 1$ because only for small $\hat{v}_{*i}$ can modes with large $\hat{k}_y$ avoid stabilization by ω_{*i}.

As explained earlier, in the regime $\hat{v}_{*i}>1$, the diamagnetic frequency ($=\hat{k}_y \hat{v}_{*i}$) and $E\times B$ shearing rate ($\sim \hat{v}_{*i}$ for the hyperbolic tangent model) both exceed the growth rate of even the fastest localized mode ($\hat{\gamma}=1$ for $\alpha \gg \alpha_c$), and as a result instability at $\hat{k}_y>1$ is no longer possible. Rather, in this regime a new pressure driven mode with $\hat{k}_y \simeq \hat{k}_x \ll 1$ appears in the system. First we note that such a long-wavelength mode can only be unstable in a localized gradient system in the limit $\alpha \gg \alpha_c$ in which the stabilizing contribution of line bending becomes relatively weak. To see this, consider modes with $\hat{k}_y \ll 1$, $\hat{k}_x \ll 1$ in the most unstable case $\hat{v}_{*i}=0$. Equation (15) then reduces to $\hat{k}_x^2 \simeq |\hat{k}_y|$, and so Eq. (14) gives $\hat{\gamma}^2 \simeq |\hat{k}_y| - \alpha_c/\alpha$, allowing instability only for $\alpha/\alpha_c > 1/|\hat{k}_y| \gg 1$. In the case of finite $\hat{v}_{*i}$, one can again solve Eq. (15) for small $\hat{k}_x$ [assuming $\tan(\hat{k}_x)\simeq \hat{k}_x$], and substitute the result into Eq. (14). Neglecting the line bending term ($=\alpha_c/\alpha$) in Eq. (14), and assuming $\hat{\gamma}_* \simeq i\hat{k}_y \hat{v}_{*i}$ on the left-hand side (the eigenfrequency of the mode will turn out to be slow compared to ω_{*i}), one then obtains (for $\hat{k}_y \ll 1$)

$$\hat{\gamma} = -i|\hat{k}_y|\hat{k}_y \hat{v}_{*i}/2 \pm (|\hat{k}_y| - \alpha_c/\alpha - \hat{k}_y^4 \hat{v}_{*i}^2/4)^{1/2}. \tag{16}$$

Maximizing the quantity inside the square root yields the most unstable wave number $\hat{k}_y = \pm \hat{v}_{*i}^{-2/3}$, and substituting this back into Eq. (16) gives the stability condition given by Eq. (2) [Fig. 1(a), dotted–dashed line]. As said earlier, given $\alpha \sim q^2 R\beta/\delta$, Eq. (2) leads to the δ-independent stability limit on the pedestal β given by Eq. (3). More generally, δ can be scaled out of the dispersion relation Eq. (16) (all terms being proportional to $\delta^{1/2}$), thus yielding an expression for the physical growth rate $\gamma(k_y)$ that is independent of the pedestal width. Introducing δ_R defined in Eq. (1) as a new normalization length scale in place of the pedestal half-width δ, and defining $\gamma_R^2 = 2P_0/(\rho_0 \delta_R R)$, Eq. (16) becomes

$$\gamma/\gamma_R = -i|k_y|k_y \delta_R^2/2 \pm (|k_y \delta_R| - (3/4)\beta_c/\beta - (k_y \delta_R)^4/4)^{1/2} \tag{17}$$

which has a maximum growth rate at $k_y \delta_R = \pm 1$ and is stable for all k_y if $\beta < \beta_c$. In addition, along the marginal stability boundary ($\beta=\beta_c$, $k_y \delta_R = \pm 1$) the mode frequency is $\gamma = \mp i\gamma_R/2$ ($\omega = \pm \gamma_R/2$), and one finds from Eq. (15) that $k_x \approx k_y$, consistent with Fig. 1(b).

Given that the asymptotic dispersion relation Eq. (17) is independent of δ, one would expect the same result could be recovered by considering the limit $\delta \to 0$ for fixed k_y and β, in which case either of the models described above approach the step profile $P = 2P_0(1-\Theta(x))$, or $\hat{P} = \hat{P}_i = \hat{\rho} = 2(1-\Theta(\hat{x}))$ (the profiles $\hat{\rho} = 2(1-\Theta(\hat{x}))$ and $\hat{\rho}=1$ turn out to yield the same result in this case). Here, we take the normalization scale δ_0 introduced in Eq. (13) to be $\delta_0 = \delta_R$ as above, in which case $\hat{v}_{*i0}=1$ and $\alpha_c/\alpha_0 = (3/4)\beta_c/\beta$. Assuming the external solution $\tilde{f} = \exp(-|\hat{k}_y||\hat{x}|)$, and integrating Eq. (13) across $x=0$, we obtain

$$\hat{\gamma}^2 + (3/4)\beta_c/\beta = -|\hat{k}_y|(i\hat{k}_y \hat{\gamma} - 1), \tag{18}$$

the solution of which is given by Eq. (17).

V. CONCLUSION

We have explored the stability of the tokamak edge pedestal to ballooning modes using three-dimensional simulations of the Braginskii equations as well a two-fluid stability analysis of some simple pedestal models. We find the impact of ion diamagnetic drift, $E\times B$ shear, and the finite radial localization of the pedestal pressure gradient on the stability of the pedestal profile depends on the ratio of δ_R/δ, where δ is the pedestal half-width and δ_R is given by Eq. (1). For $\delta_R/\delta<1$, the stability boundary of the model profiles arise from the onset of short wavelength ($k_\theta \delta < 1$) ballooning modes that are radially localized to the steep gradient region, and is essentially the same as that obtained from local, ideal MHD theory. In this case (which might apply to larger machines given that δ_R scales only as $R^{1/3}$), the maximum stable β value in the pedestal $\beta \sim (\alpha_c/q^2)\delta/R$ depends on the pedestal width, and thus cannot be determined uniquely from stability considerations alone. In the limit $\delta_R/\delta>1$, on the other hand, conventional ballooning modes localized within the pedestal region become stable, and the pedestal pressure gradient can far exceed the critical gradient obtained from local MHD theory. In this case, the stability of the pedestal profile is limited by the onset of an ideal, pressure driven ''surface'' instability that depends only on the pressure drop across the pedestal. The stability of this mode imposes a limit on the pedestal β given by Eq. (3), and thus, in contrast to the case $\delta_R/\delta<1$, the maximum pedestal β can be determined even though the pedestal width is unspecified. Near marginal conditions the limiting mode has a real frequency $\omega \sim c_s/\sqrt{\delta_R R}$ that is small compared to ω_{*i} in the pedestal (it may therefore be sensitive to our assumption that the $E\times B$ and ion diamagnetic drifts precisely balance in the pedestal). It also has a poloidal wave number $k_\theta \sim 1/\delta_R$ and a radial envelope $\sim \delta_R$ that are much larger than the pedestal width. Since the maximum stable value of α/α_c in this regime [see Eq. (2)] is $\alpha/\alpha_c \sim \delta_R/\delta$, this implies, in the regime where α/α_c becomes large, that the radial penetration depth of the edge limiting linear instability ($\sim \delta_R$) relative to the pedestal width ($\sim \delta$) increases as $\alpha/\alpha_c \gg 1$. Assuming the linear and nonlinear radial mode widths are comparable (which need not be the case[5]), this would imply edge localized modes in the $\alpha/\alpha_c \gg 1$ regime would have a more devastating impact on the edge pressure profile.

[1] R. J. Groebner and T. H. Osborne, Phys. Plasmas **5**, 1800 (1998).
[2] F. L. Hinton and G. M. Stabler, Phys. Fluids B **5**, 1281 (1993).
[3] B. N. Rogers, J. F. Drake, and A. Zeiler, Phys. Rev. Lett. **81**, 4396 (1998).
[4] A. Zeiler, D. Biskamp, J. F. Drake, and P. N. Guzdar, Phys. Plasmas **3**, 2951 (1996).
[5] O. A. Hurricane, B. H. Fong, and S. C. Cowley, Phys. Plasmas **4**, 3565 (1997).